Supported Iron Nanoparticles as Catalysts for Sustainable Production of Lower Olefins

Hirsa M. Torres Galvis, *et al.*

Science **335**, 835 (2012);
DOI: 10.1126/science.1215614

This copy is for your personal, non-commercial use only.

Supported Iron Nanoparticles as Catalysts for Sustainable Production of Lower Olefins

Hirsa M. Torres Galvis,[1] Johannes H. Bitter,[1] Chaitanya B. Khare,[2] Matthijs Ruitenbeek,[2] A. Iulian Dugulan,[3] Krijn P. de Jong[1]*

Lower olefins are key building blocks for the manufacture of plastics, cosmetics, and drugs. Traditionally, olefins with two to four carbons are produced by steam cracking of crude oil–derived naphtha, but there is a pressing need for alternative feedstocks and processes in view of supply limitations and of environmental issues. Although the Fischer-Tropsch synthesis has long offered a means to convert coal, biomass, and natural gas into hydrocarbon derivatives through the intermediacy of synthesis gas (a mixture of molecular hydrogen and carbon monoxide), selectivity toward lower olefins tends to be low. We report on the conversion of synthesis gas to C_2 through C_4 olefins with selectivity up to 60 weight percent, using catalysts that constitute iron nanoparticles (promoted by sulfur plus sodium) homogeneously dispersed on weakly interactive α-alumina or carbon nanofiber supports.

Lower olefins (C_2 to C_4) are extensively used in the chemical industry as building blocks to synthesize a wide range of products such as polymers, solvents, drugs, cosmetics, and detergents. Traditionally, lower olefins have been produced by thermal or catalytic cracking of naphtha or vacuum gas oil (1) or from dehydrogenation of alkanes (2, 3), but environmental and economic factors are currently spurring exploration of alternative routes for their production.

In recent years there has been growing interest in the development of biomass as a renewable feedstock for the production of commodity compounds (4, 5). Pyrolized biomass or bio-oil can be converted catalytically to lower olefins with moderate selectivity (43% C) (5), although other compounds such as aromatics are also produced. Schemes put forward to produce lower olefins from synthesis gas (syngas)—a mixture of H_2 and CO obtained through biomass gasification—

consist of at least two conversion steps, which involve either cracking of Fischer-Tropsch (FT)–derived hydrocarbons (6) or the methanol to olefins (MTO) process (7). Here, we consider Fischer-Tropsch to olefins (FTO) as a direct route, without intermediate steps, to transform syngas into light olefins.

For several decades, research groups have attempted to develop iron-based catalysts to direct product selectivity of the FT synthesis toward light olefins (8, 9). Relative to other FT catalysts such as cobalt, iron disfavors competing formation of methane, and furthermore catalyzes the water-gas shift reaction, enabling the use of a CO-rich syngas feed without an H_2/CO ratio adjustment. Mainly unsupported (sometimes referred to as bulk) iron oxide catalysts have been investigated (9–12), and in some cases they have exhibited high selectivities toward lower olefins (up to 70 wt %) when the iron was modified by the addition of promoters (9). Despite these promising results, however, the bulk iron catalysts are mechanically unstable when the reaction is performed at high temperature, which is necessary to steer product selectivity to lighter hydrocarbons. Under these conditions, the undesirable Boudouard reaction, $2CO(g) \rightarrow C(s) + CO_2(g)$ (13), leads to the deposition of carbon, which

can block the active sites and induce fragmentation of the particles in bulk iron catalysts (14). The poor mechanical stability of the bulk iron oxide catalysts may lead to plugging of the catalyst bed in fixed-bed operation or to fouling of separation equipment in a fluidized-bed process.

Supported iron catalysts display enhanced dispersion of the active phase and may withstand the mechanical degradation that threatens bulk iron catalysts. Research on supported iron catalysts (15–21) has met with limited success, however. Barrault et al. (15) found that iron dispersed on alumina with high surface area displayed much lower activity than did iron dispersed on alumina with low surface area. This finding points to a key aspect of supported iron catalysts—that is, their cumbersome activation. If highly dispersed iron oxide interacts strongly with an oxidic support with high surface area, the conversion of iron oxide into the active phase (iron carbide) is impeded (14). Other supports for iron-based FTO catalysts in addition to alumina (15, 16) have been explored, such as zeolites (18), aluminophosphate molecular sieves (19), and carbonaceous materials (20, 21). Table S1 summarizes the most relevant results reported in the literature regarding the development of carbon- or alumina-supported iron catalysts for the selective production of lower olefins. Iron supported on activated carbon displayed a high catalytic activity, but this was accompanied by low selectivity to light olefins (20) or a high deactivation rate (21). Many years of research have shown that supported iron catalysts display an inverse relationship between activity and selectivity (15).

To overcome the low activity and mechanical stability problems, we explored the use of support materials weakly interactive toward iron. As a working hypothesis, we posited that these inert supports would impart mechanical stability to the iron nanoparticles without inhibiting their activation. In particular, nanostructured carbon materials (22), such as carbon nanofibers (CNF) (23, 24) and carbon nanotubes (25), boast high specific surface area, chemical inertness, and good mechanical strength.

In addition to CNF, we explored β-silicon carbide (β-SiC) and α-alumina (α-Al_2O_3) as supports. For comparison, we also examined three bulk

[1]Inorganic Chemistry and Catalysis, Debye Institute for Nanomaterials Science, Utrecht University, P.O. Box 80083, 3508 TB Utrecht, Netherlands. [2]DOW Benelux B.V., P.O. Box 48, 4530 AA Terneuzen, Netherlands. [3]Fundamental Aspects of Materials and Energy Group, Delft University of Technology, 2629 JB Delft, Netherlands.

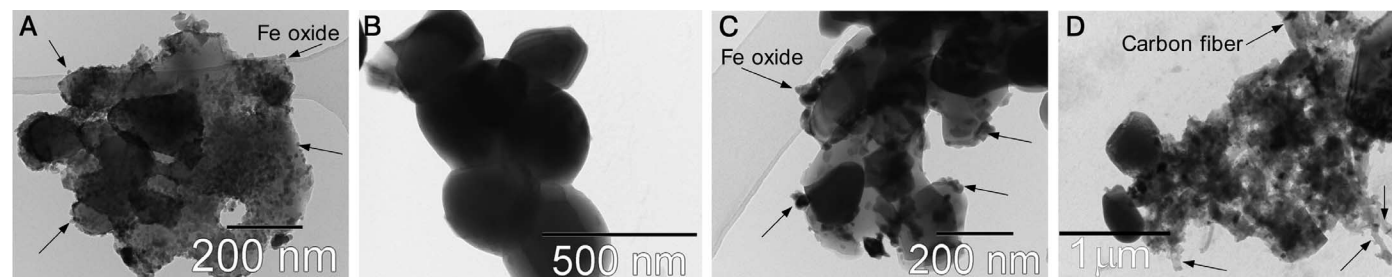*To whom correspondence should be addressed. E-mail: k.p.dejong@uu.nl

Fig. 1. TEM images of fresh and spent Fe catalysts. (**A** and **B**) The images from the fresh Fe/α-Al_2O_3 catalysts (A) show a homogeneous distribution of iron oxide nanoparticles on the support, whereas the bulk Fe-Ti-Zn-K catalyst (B) is mainly composed of aggregates of iron oxide crystals. (**C** and **D**) In images of the spent catalysts after 64 hours of reaction at 340°C, 20 bar, and a H_2/CO ratio of 1, the Fe/α-Al_2O_3 (C) showed sintering of Fe particles after reaction; the bulk spent catalyst (D) fragmented and manifested carbon fiber growth (indicated by arrows).

iron catalysts (one unpromoted and two promoted) and iron supported on conventional high-surface-area SiO_2 and γ-Al_2O_3. The supported Fe catalysts were prepared using ammonium iron citrate as precursor with a nominal iron loading of 10 wt %, whereas the bulk catalysts had an iron content higher than 30 wt % (table S2). The ammonium iron citrate used in the preparation of the supported samples contained low amounts of sulfur and sodium and efficiently introduced these promoters in the catalysts (table S3).

The use of ammonium iron citrate as the metal precursor provides a homogeneous distribution of the iron nanoparticles on the support, in contrast to the extensive clustering that is observed when using iron nitrate (26). Fe nanoparticle aggregation could lead to low catalytic activity and high methane selectivity, as observed when using bulk iron catalysts. Transmission electron microscopy (TEM) was used to determine the size of the iron oxide particles and their distribution on the support.

Figure 1A shows a representative TEM micrograph of the calcined Fe/α-Al_2O_3, which exhibited a homogeneous distribution of iron oxide particles (arrows). The Fe_2O_3 particle size distribution (fig. S2) was 14 ± 5 nm on this support and 5 ± 1 nm on CNF. The bulk promoted catalyst

(Fe-Ti-Zn-K) consisted of large Fe_2O_3 particles (average size 400 nm), which formed aggregates resembling grape bunches (Fig. 1B).

The volume-averaged Fe_2O_3 crystallite size of the Fe catalyst precursors was calculated with the Scherrer equation using the parameters obtained by x-ray diffraction analysis (fig. S3 and table S2). Fe/SiO_2, Fe/γ-Al_2O_3, and Fe/β-SiC did not show the characteristic diffraction lines from iron oxide, indicating that the Fe_2O_3 was amorphous or that the crystallites were smaller than 4 nm (fig. S3).

The fresh catalysts were also analyzed by Mössbauer spectroscopy to determine the composition of the iron phase (tables S4 and S5). Iron was present in the form of hematite (α-Fe_2O_3) in all samples. A superparamagnetic (SPM) iron oxide phase (α-Fe_2O_3 SPM) was measured in Fe_2O_3 particles smaller than 13.5 nm (table S4 and accompanying text). Iron was highly dispersed on CNF, γ-Al_2O_3, and SiO_2, as evidenced by the presence of SPM nanoparticles exclusively. The iron oxide particles on α-Al_2O_3 and β-SiC had a broader size distribution, whereas the bulk Fe-Ti-Zn-K catalyst was primarily composed of large Fe_2O_3 particles.

The supported and bulk Fe catalysts were tested in the FT reaction at 1 bar and 350°C at

low CO conversion (0.5 to 1%) to restrict secondary hydrogenation of olefins (Table 1 and fig. S4). Catalytic activity is expressed as iron time yield (i.e., the number of CO moles converted to hydrocarbons per gram of iron per second). A high initial activity was observed for Fe/β-SiC and Fe/CNF. The activity of Fe/CNF decreased continuously during the 15 hours of reaction; the activity of the Fe/β-SiC catalyst increased during the first 5 hours of reaction, then decreased slowly afterward (fig. S4A). Fe/α-Al_2O_3 exhibited a lower catalytic activity than Fe/CNF and Fe/β-SiC; however, it showed remarkable stability, as the activity remained constant over 15 hours. Fe/γ-Al_2O_3 and Fe/SiO_2 displayed a low catalytic activity, comparable to the bulk Fe catalysts (fig. S4B). The Fe-Cu-K-SiO_2 catalysts showed an initial activity approximately 4 times that of the Fe-Ti-Zn-K catalyst. Nevertheless, the iron time yield decreased rapidly to achieve comparable values after 15 hours of reaction.

One of the most important requirements for an FTO catalyst is to obtain the maximum production of the lower-olefins fraction while limiting methane selectivity to the lowest level possible. Fe/CNF and Fe/α-Al_2O_3 exhibited high selectivity toward lower olefins (~60% C) while directing comparatively little carbon to methane (<25% C)
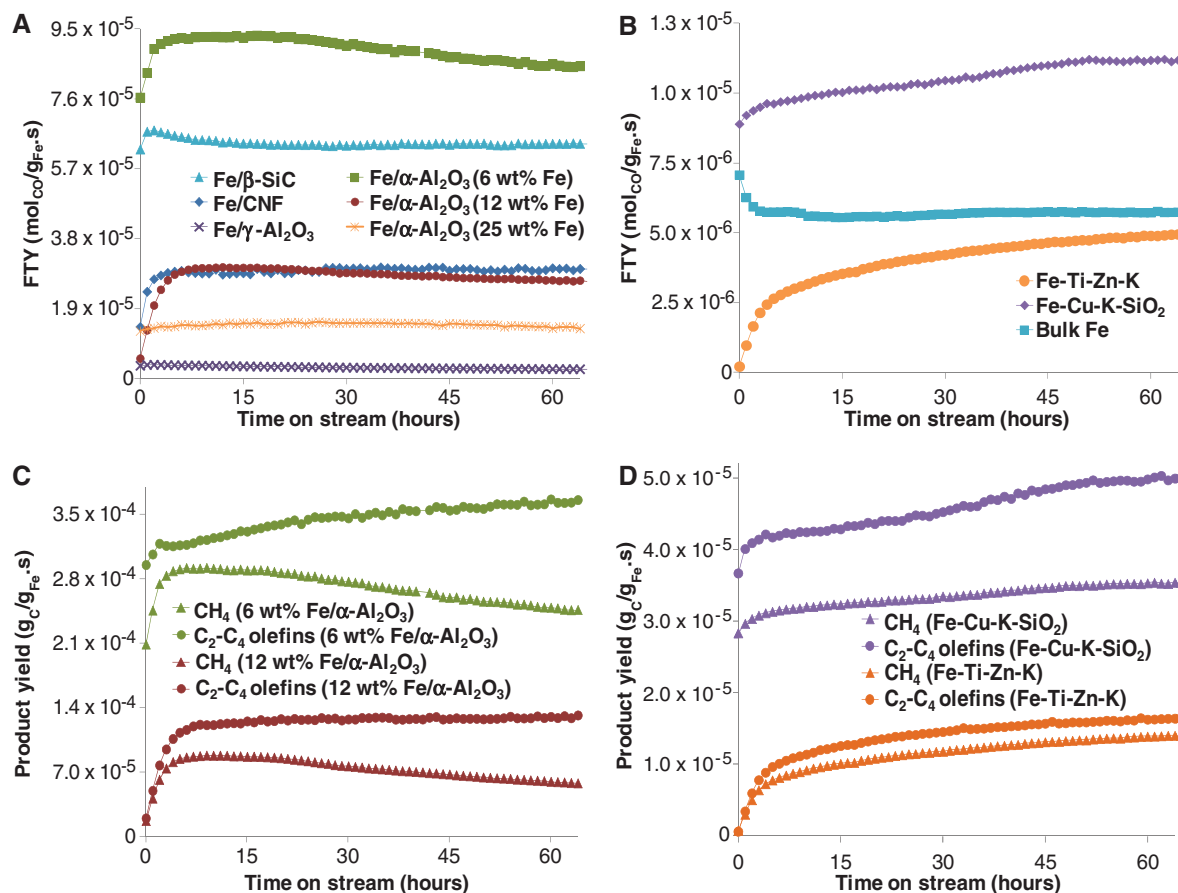
Fig. 2. (A to D) Catalytic performance of iron catalysts for the FTO process at 20 bar. Catalytic tests were carried out at T = 340°C, P = 20 bar, and a H_2/CO ratio of 1. Iron time yield is plotted above as a function of time for (C) Fe-supported catalysts and (B) bulk Fe catalysts. Methane and lower olefins yields are plotted below as a function of time for (C) Fe-supported catalysts and (D) bulk Fe catalysts. The product yields were obtained at CO conversion levels between 70 and 80%.

(Table 1). Fe/β-SiC and Fe/SiO$_2$ also showed high selectivity to C$_2$ through C$_4$ olefins, but the CH$_4$ product fraction was higher than 30% C. Fe/γ-Al$_2$O$_3$ and the bulk catalysts displayed a high selectivity to methane (>40% C), which is not desirable for their application in the FTO process.

Additional tests were carried out at 20 bar, 340°C, and an H$_2$/CO ratio of 1 to observe the performance of supported and bulk Fe catalysts under industrially relevant conditions (Fig. 2). In view of the promising results obtained at 1 bar, we prepared and tested additional α-Al$_2$O$_3$–supported catalysts with different iron loadings (6 and 25 wt % Fe) to study the effect of iron content on catalytic performance. Most of the catalysts showed an initial increase in activity, except for the un-promoted bulk Fe (Fig. 2B), which exhibited a decrease in activity during the first 10 hours of reaction before reaching stability. After an initial activation period, Fe/β-SiC, Fe/CNF, 25 wt % Fe/α-Al$_2$O$_3$, and Fe/γ-Al$_2$O$_3$ showed a stable catalytic activity for 60 hours. A slight decrease in activity during reaction was observed for the 6 wt % and 12 wt % Fe/α-Al$_2$O$_3$ catalysts, mainly resulting from a continuous drop in CH$_4$ production (Fig. 2C). The stability maintained during 60 hours fully complies with the requirements for the application of these catalysts in fluidized-bed reactors. In view of their favorable heat transfer characteristics, it is expected that these reactors will be preferred in industrial applications of the exothermic FTO process.
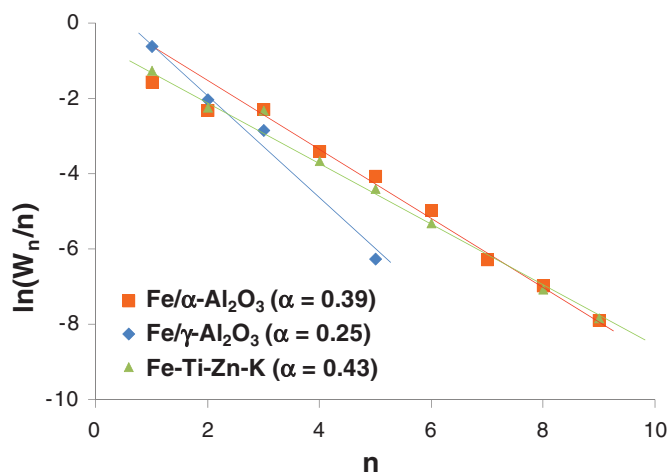
Table 2 summarizes the activities and product selectivities measured after 64 hours of reaction at 20 bar. The CO$_2$ selectivity for all the samples was approximately 40% on the basis of CO converted, except for Fe/γ-Al$_2$O$_3$ (table S6). Under the selected reaction conditions, most of the catalysts had comparable CO conversion levels (77 to 81%; table S6). However, the Fe/γ-Al$_2$O$_3$ catalyst only achieved a CO conversion of 10%. The promoted catalysts prepared using supports with low interaction with iron showed high catalytic activities combined with high selectivities to the desired products. Fe/CNF and 25 wt % Fe/α-Al$_2$O$_3$ exhibited high selectivities toward C$_2$ through C$_4$ olefins (>50% C) while yielding a methane product fraction lower than 15% C. The Fe-Cu-K-SiO$_2$ catalyst showed a catalytic activity comparable to the 25 wt % Fe/α-Al$_2$O$_3$; however, only moderate selectivities toward lower olefins were obtained.

The Anderson-Schulz-Flory model (eq. S2) that is used to predict the product distribution indicates that the maximum selectivity achievable for the C$_2$-C$_4$ fraction, including olefins and paraffins, is approximately 50 wt %, at a chain growth probability (α) between 0.4 and 0.5, as shown in fig. S5. This model predicts that methane selectivity is about 30 wt % when this maximum C$_2$-C$_4$ selectivity is reached.

Anderson-Schulz-Flory (ASF) plots (Fig. 3 and fig. S6) show that the catalysts prepared using inert supports provide α values of ~0.4, close to the optimal value for maximum lower-olefins production. Moreover, the plots in Fig. 3 revealed lower methane selectivities relative to the values predicted from the ASF model. This can be rationalized from the simplified "surface carbide" or "alkyl" mechanism (fig. S1), which is widely accepted for the FT synthesis (13). In this model, following CO dissociation and carbon hydrogenation, a CH$_3$ group adsorbed on the catalyst surface is proposed to act as a chain initiator. The carbon chain grows by the addition of methylene monomer units (CH$_2$) to the adsorbed alkyl species. The chain growth is terminated by β-hydride abstraction to form α-olefins or by hydrogenation to produce paraffins. Negative deviations from the ASF prediction for methane selectivity can be expected when using iron catalysts modified

Table 1. Product selectivity and catalytic activity at 1 bar. Catalytic tests were performed at 350°C and a H$_2$/CO ratio of 1; results after 15 hours on stream are shown (CO conversion: 0.5 to 1.0%). The product mixture that was analyzed consisted of C$_1$ to C$_{16}$ hydrocarbons. Iron time yield (FTY) represents moles of CO converted to hydrocarbons per mol of Fe per second; %C is defined as carbon atoms in a product with respect to the total number of C atoms in the hydrocarbon mixture. CO$_2$ was not measured.

Sample	FTY (10^{-6} mol$_{CO}$/g$_{Fe}$.s)	Selectivity (%C)			
		CH$_4$	C$_2$–C$_4$ olefins	C$_2$–C$_4$ paraffins	C$_{5+}$
Fe/CNF	1.41	23	61	4	12
Fe/α-Al$_2$O$_3$ (12 wt % Fe)	0.65	22	61	4	13
Fe/β-SiC	6.52	31	58	4	7
Fe/SiO$_2$	0.14	38	56	5	1
Fe/γ-Al$_2$O$_3$	0.07	54	44	2	0
Fe-Ti-Zn-K	0.13	83	16	1	0
Fe-Cu-K-SiO$_2$	0.20	43	46	2	9
Bulk Fe	0.08	76	21	2	1

Table 2. Catalytic performance at 20 bar. Catalytic tests were performed at 340°C and a H$_2$/CO ratio of 1; results after 64 hours on stream are shown. The product mixture that was analyzed consisted of C$_1$ to C$_{10}$ hydrocarbons. FTY and selectivity are defined as in Table 1. The selectivities were calculated on hydrocarbons produced; CO conversions and CO$_2$ selectivities are reported in table S6.

Sample	FTY (10^{-5} mol$_{CO}$/g$_{Fe}$.s)	Selectivity (%C)				
		CH$_4$	C$_2$–C$_4$ olefins	C$_2$–C$_4$ paraffins	C$_{5+}$	Oxygenates
Fe/CNF	2.98	13	52	12	18	5
Fe/α-Al$_2$O$_3$ (6 wt % Fe)	8.48	24	35	21	10	10
Fe/α-Al$_2$O$_3$ (12 wt % Fe)	2.66	17	39	19	14	11
Fe/α-Al$_2$O$_3$ (25 wt % Fe)	1.35	11	53	6	21	9
Fe/β-SiC	6.38	35	19	39	4	3
Fe/γ-Al$_2$O$_3$	0.25	49	33	11	1	6
Fe-Ti-Zn-K	0.49	24	28	29	10	9
Fe-Cu-K-SiO$_2$	1.12	26	36	12	18	8
Bulk Fe	0.57	30	32	18	14	6

Fig. 3. Comparison of ASF plots for supported and bulk catalysts. The ASF plots are based on the product distribution obtained when performing the FT reaction at 20 bar, 340°C, and a H$_2$/CO ratio of 1 after 64 hours time on stream. Fe/α-Al$_2$O$_3$ has an iron loading of 12 wt %; n is the number of carbon atoms in a product, and W_n is the weight fraction of the product with carbon number equal to n.

Fe/α-Al$_2$O$_3$ (α = 0.39)
Fe/γ-Al$_2$O$_3$ (α = 0.25)
Fe-Ti-Zn-K (α = 0.43)

with promoters that limit the hydrogenation reactions (8), thus favoring chain growth and the termination step via β-hydride abstraction that cannot give rise to CH$_4$ production. The suppression of the methanation reaction induced by the promoters was only observed when using CNF or α-Al$_2$O$_3$ because these "inert" supports are thought to favor the proximity between iron and promoters (Na plus S), in contrast to reactive supports such as γ-Al$_2$O$_3$ that lead to more methane (Fig. 3). In the case of the bulk catalysts, CH$_4$ selectivities coincided with the values predicted by the ASF model or were slightly above.

Mössbauer spectroscopy of the spent catalysts after reaction at 1 bar (table S5) showed that the nature of the iron phases varied when using different support materials. Although some of the iron carbides may be oxidized after exposure to air, Fe$_x$C$_y$ was detected on the samples with moderate to high catalytic activity. In contrast, the samples with the lowest catalytic activity, Fe/SiO$_2$ and Fe/γ-Al$_2$O$_3$, did not contain any carbides. A strong metal-support interaction clearly inhibits the formation of catalytically active iron carbides, as observed for conventional high-surface-area support materials. Note that in the size range of iron particles dispersed on inert supports (7 to 20 nm), particle size effects seem to be minimal.

TEM performed on spent catalysts revealed that the iron nanoparticles in the supported samples increased in size. The particle size distributions of the fresh and spent Fe/α-Al$_2$O$_3$ and Fe/CNF are shown in fig. S2. For Fe/CNF, changes in the catalytic activity were only observed during the first 4 hours of reaction, which suggests that the changes in the catalyst structure took place during catalyst activation and initial usage. In the case of Fe/α-Al$_2$O$_3$, the average iron nanoparticle size increased from 14 ± 5 nm to 17 ± 5 nm (Fig. 1C). The promoted bulk iron oxide showed

extensive particle fragmentation and carbon filament growth, which brings about the poor mechanical stability of this catalyst (Fig. 1D).

The spent catalysts were characterized with thermogravimetric analysis to determine the extent of carbon lay-down. Carbon burn-off experiments were performed for all the samples, except for the Fe/CNF catalyst. Although extensive carbon deposition on the samples after reaction with CO-rich syngas and high temperatures could be expected, most of the samples exhibited low solid carbon formation. After 64 hours of reaction at 340°C and 20 bar, the levels of carbon lay-down measured on the spent catalysts were lower than 10 wt %. In contrast, Fe/α-Al$_2$O$_3$ (25 wt % Fe) and Fe-Cu-K-SiO$_2$ exhibited a higher extent of coke formation (23 wt % and 40 wt %, respectively).

The FTO process represents a strong alternative route for the sustainable production of lower olefins from biomass-derived synthesis gas. The industrial potential of this process is greatly enhanced by the reported development of active, selective, and mechanically stable catalysts that consist of promoted iron nanoparticles dispersed on weakly interactive supports. Further suppression of methane production, maximization of the C$_2$-C$_4$ olefins fraction, and reduction of carbon lay-down by addition of promoters and by optimization of physical properties (e.g., Fe particle size, distribution of Fe nanoparticles on the support) will allow us to further understand and develop the performance of these catalysts.

References and Notes

1. A. Corma, F. V. Melo, L. Sauvanaud, F. Ortega, *Catal. Today* **107–108**, 699 (2005).
2. R. Diercks *et al.*, *Chem. Eng. Technol.* **31**, 631 (2008).
3. S. Wang, Z. H. Zhu, *Energy Fuels* **18**, 1126 (2004).
4. E. L. Kunkes *et al.*, *Science* **322**, 417 (2008).
5. T. P. Vispute, H. Zhang, A. Sanna, R. Xiao, G. W. Huber, *Science* **330**, 1222 (2010).
6. X. Dupain, R. A. Krul, C. J. Schaverien, M. Makkee, J. A. Moulijn, *Appl. Catal. B* **63**, 277 (2006).
7. G. A. Olah, *Angew. Chem. Int. Ed.* **44**, 2636 (2005).
8. C. Wang, L. Xu, Q. Wang, *J. Nat. Gas Chem.* **12**, 10 (2003).
9. B. Büssemeier, C. D. Frohning, G. Horn, W. Kluy, U.S. Patent 4564642 (1986).
10. B. H. Davis, *Catal. Today* **84**, 83 (2003).
11. S. Soled, E. Iglesia, R. A. Fiato, *Catal. Lett.* **7**, 271 (1990).
12. Y. Jin, A. K. Datye, *J. Catal.* **196**, 8 (2000).
13. A. P. Steynberg, M. E. Dry, Eds., *Fischer-Tropsch Technology* (Elsevier, Amsterdam, 2004).
14. M. D. Shroff *et al.*, *J. Catal.* **156**, 185 (1995).
15. J. Barrault, C. Forquy, J. C. Menezo, R. Maurel, *React. Kinet. Catal. Lett.* **15**, 153 (1980).
16. B. G. Baker, N. J. Clark, H. MacArthur, E. Summerville, U.S. Patent 4610975 (1986).
17. D. B. Bukur *et al.*, *Ind. Eng. Chem. Res.* **29**, 1588 (1990).
18. L. Xu, Q. Wang, Y. Xu, J. Huang, *Catal. Lett.* **31**, 253 (1995).
19. M. L. Cubeiro *et al.*, *Appl. Catal. A* **167**, 183 (1998).
20. V. K. Jones, L. R. Neubauer, C. H. Bartholomew, *J. Phys. Chem.* **90**, 4832 (1986).
21. A. P. B. Sommen, F. Stoop, K. van der Wiele, *Appl. Catal.* **14**, 277 (1985).
22. K. P. de Jong, *Oil Gas Sci. Technol.* **61**, 527 (2006).
23. K. P. de Jong, J. W. Geus, *Catal. Rev., Sci. Eng.* **42**, 481 (2000).
24. E. van Steen, F. F. Prinsloo, *Catal. Today* **71**, 327 (2002).
25. W. Chen, Z. Fan, X. Pan, X. Bao, *J. Am. Chem. Soc.* **130**, 9414 (2008).
26. A. J. van Dillen, R. J. A. M. Terörde, D. J. Lensveld, J. W. Geus, K. P. de Jong, *J. Catal.* **216**, 257 (2003).

Plate Motions and Stresses from Global Dynamic Models

Attreyee Ghosh* and William E. Holt

Delineating the driving forces behind plate motions is important for understanding the processes that have shaped Earth throughout its history. However, the accurate prediction of plate motions, boundary-zone deformation, rigidity, and stresses remains a difficult frontier in numerical modeling. We present a global dynamic model that produces a good fit to such parameters by accounting for lateral viscosity variations in the top 200 kilometers of Earth, together with forces associated with topography and lithosphere structure, as well as coupling with mantle flow. The relative importance of shallow structure versus deeper mantle flow varies over Earth's surface. Our model reveals where mantle flow contributes toward driving or resisting plate motions. Furthermore, subducted slabs need not act as strong stress guides to satisfy global observations of plate motions and stress.

Predicting plate motions correctly, along with stresses within the plates, has been a challenge for global dynamic models. Accurate predictions are vitally important for understanding the forces responsible for the movement of plates, mountain building, rifting of continents,

and strain accumulation released in earthquakes. Previous studies have investigated these driving forces by either predicting stresses in the plates alone (*1, 2*) or plate motions alone (*3–5*). Other studies have taken the important step of predicting both plate motions and stresses in a single model (*6–8*). However, in addition to predicting plate motions, a successful global dynamic model must also explain plate rigidity and plate boundary-zone deformation, as well as intraplate stress patterns. Furthermore, the presence of lateral viscosity variations within the top 200 km of Earth influences the coupling between lithosphere and mantle convection. A systematic investigation of this influence is needed to improve our understanding of the driving mechanisms for plate tectonics.

Geosciences Department, Stony Brook University, Stony Brook, NY 11794, USA.

*To whom correspondence should be addressed. E-mail: atreig@gmail.com